NRC Research Press

ARTICLE

Experimental investigation on stainless steel welding with a 15 kW fibre laser

M. Foster, R. Beaulieu, L. Blais, G. Caron, and M. Langlois

Abstract: In the present study, attenuation of the laser beam because of the induced plume during bead-on-plate welding of an austenitic stainless steel plate with a 15 kW fibre laser beam, was investigated to better understand laser welding phenomena. A high-speed video camera was used to monitor the plume and keyhole behaviour. Attenuation and refraction levels, due to the induced plume, were measured by different wavelengths laser probes. Finally, a high resolution spectrometer was used to analyze spectral emission from the induced plasma plume by the fibre laser beam. The Boltzmann plot method was used to estimate the temperature of laser-induced plasma plume and Saha's equation was applied to calculate the ionization degree.

PACS No.: 42.62.Cf.

Résumé : Afin de mieux comprendre le mécanisme du soudage par laser, nous étudions ici l'atténuation d'un faisceau laser due au panache formé lors d'une soudure sur une plaque d'acier inoxydable austénitique à l'aide d'un laser à fibre de 15 kW. Une caméra haute vitesse a enregistré le comportement du panache et du capillaire de vaporisation (keyhole). Nous avons mesuré l'atténuation et la réfraction engendrées par le panache à l'aide de sondes laser de différentes longueurs d'onde. Finalement, un spectromètre à haute résolution nous permet d'analyser le spectre d'émission du panache de plasma généré par le faisceau du laser à fibre. Nous utilisons la méthode de Boltzmann pour déterminer la température du plasma et l'équation de Saha pour estimer le degré d'ionisation. [Traduit par la Rédaction]

1. Introduction

When an infrared laser beam hits a solid metal target, the major part of the laser beam radiation is reflected at the target surface while the rest is absorbed [1–7]. This absorption depends on the laser wavelength and on the nature of the metal. For 1.07 μm wavelength fiber laser, the absorption is about 30%–40% on steel [2, 5–7]. In metal, the radiation is extremely rapidly absorbed by electronic thermalization at the target surface [1, 2, 6–8]. The material is heated, undergoes a melting process at 1–10 kW/mm² while undergoing a vaporization process at 10–100 kW/mm², which leads to the creation of a keyhole [6–8]. The pressurized vapor phase maintains the keyhole opening. The laser passes through this vapor and is partially absorbed at the keyhole wall by Fresnel absorption. The laser power is absorbed and reflected at the wall multiple times toward the bottom of the keyhole, thus enhancing the penetration into the material. For a constant instrumental setup and welding speed, this penetration mainly depends on the laser power input. When the laser power density exceeds 0.1–10 MW/mm², the vapor formed in the keyhole progresses to an ionization state by collisions between thermal electrons [3, 6–8]. This ionization leads to a laser enhanced plasma formation in the keyhole. This keyhole plasma expands from the surface along the incoming laser beam to form a plasma plume by the mixture of the metallic gas with the ambient gases trapped on the surface by the Venturi effect [6, 7]. Keyhole plasma and plasma plume absorb the laser beam, mainly by inverse Bremsstrahlung (IB) [1, 3, 5–10]. This absorption reduces the amount of laser power at the bottom of the keyhole, thus decreasing the penetration. During the welding process, the liquid of the turbulent melt pool flows around the keyhole toward the pool tail [3, 4, 9]. An amount of the molten metal, depending on the weld speed and the liquid velocity, is expelled by vapor ejection to generate droplet projections [6, 7, 9]. Meanwhile, the vapor ejection generates a fume that ignites in the path of the laser beam [10]. This ignited fume, commonly called plume, is the result of the combustion of the ejected metallic gas that absorbs the laser energy input. The compressed gas, generated in the keyhole, is expelled at the top of the keyhole and condenses in very fine particles at ambient temperature and pressure [1, 6–8]. These fine metallic particles diffuse and absorb the laser beam and create a flame when they undergo oxidation with O_2 from the air. Therefore, several factors, such as refraction, scattering, and absorption should be considered when characterizing plume induced by a 15 kW fiber laser beam.

Several papers concerning steel and stainless steel welding with a near-infrared wavelength laser have been published. Dumord et al. [11] studied the laser–matter interaction during CW 2 kW Nd:YAG laser welding of an austenitic stainless steel. They showed that the plume scatters the laser beam and causes a nail-head shape of the welding seam. They measured a plume temperature close to the boiling point of steel; the plume consisting of vapor, gas, and microdroplets. They concluded that, when using a near-infrared laser, IB absorption by the plasma plume above the keyhole is low when compared to the CO_2 laser welding process and therefore, absorption phenomena in the keyhole are regulated by the Fresnel absorption. Also, Lacroix et al. [12] confirmed by a more detailed study that the nail-head shape of the welding seam is caused by Mie scattering and that there is no plasma plume shielding and defocussing during welding with a 1 kW Nd:YAG laser.

Greses et al. [13] studied the plume attenuation when welding mild steel with CW 8 kW Nd:YAG and 3.5 kW CO_2 lasers. They

Received 14 December 2012. Accepted 19 September 2013.

M. Foster, L. Blais, and G. Caron. Novika Solutions, 129, rue du Parc-de-l'Innovation, La Pocatière, QC G0R 1Z0, Canada.
R. Beaulieu. Cégep de La Pocatière,140, 4e Avenue, La Pocatière, QC G0R 1Z0, Canada.
M. Langlois. OPTECH,129, rue du Parc-de-l'Innovation, La Pocatière, QC G0R 1Z0, Canada.
Corresponding author: M. Foster (e-mail: mfoster@novika.ca).

Fig. 1. Schematic diagram of the experimental set up.

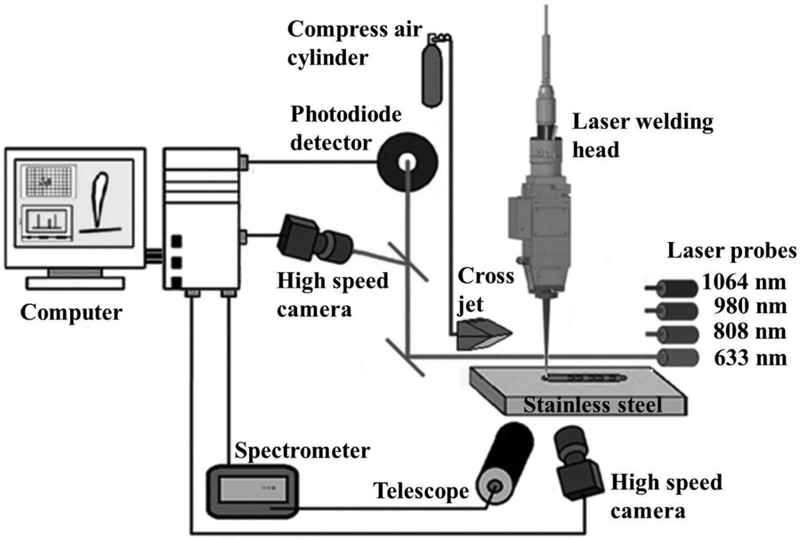

Fig. 2. High-speed images showing the laser-induced plume behaviour and spatters generation.

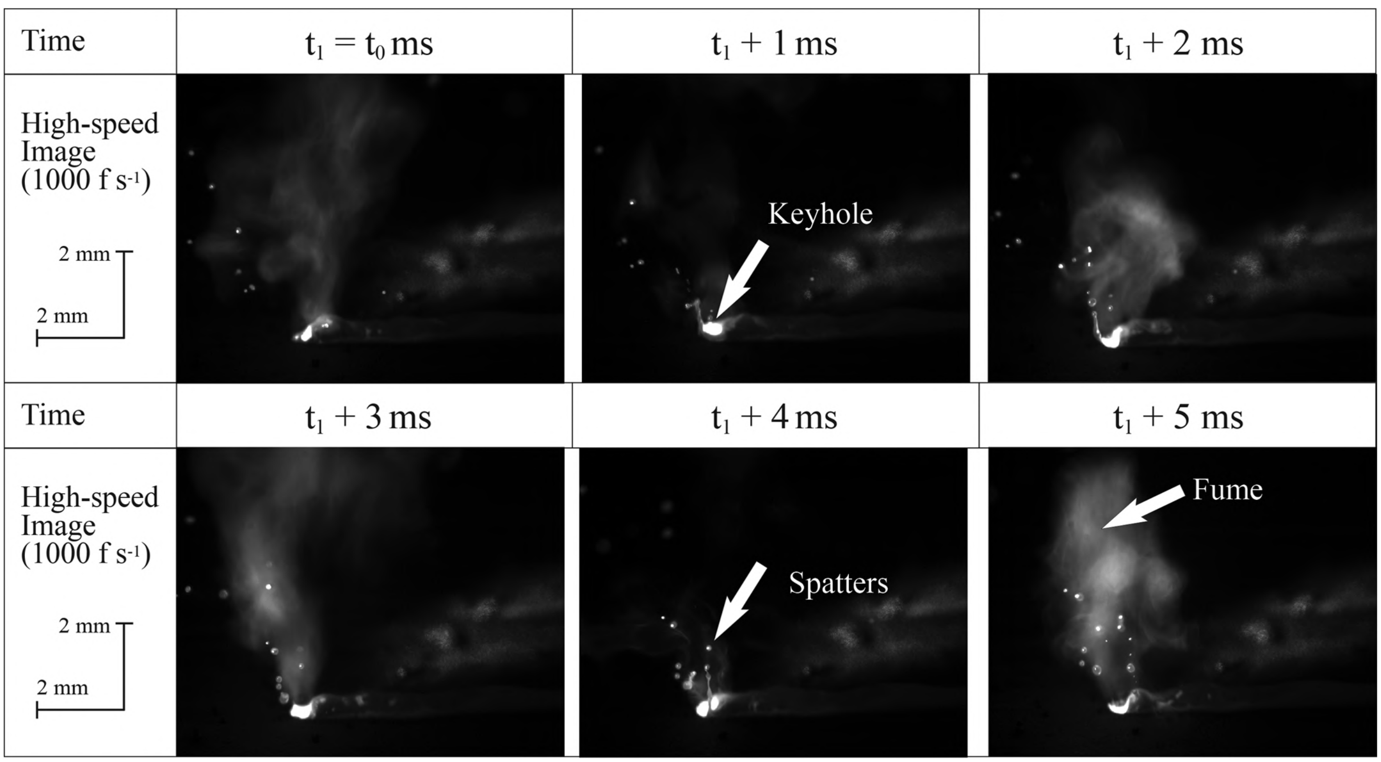

compared the granulometric distribution of the particles of the plume for both lasers at 3.5 kW in Ar–air and He–air environments. They found that the average size of the particles is less than 50 nm for Nd:YAG welding plume and smaller than 4 nm for CO_2 welding plume. Those results confirm that Rayleigh scattering causes laser beam diffusion and defocussing.

Katayama et al. [14–17] investigated characteristics of a laser-induced plume during the laser welding process of 304 stainless steel plates with a 10 kW fibre laser. The authors reported that during the weld, weakly ionized plasma was formed. The main attenuation factor is attributed to Rayleigh's scattering. They also reported that the laser-induced plasma plume interaction was too small to reduce weld penetration. They concluded in another study that without shielding gas, a plume higher than 20 mm affects the refractive index of the air along the path of the laser beam [18]. These variations of the refractive index defocus and refract the laser beam and decrease the laser beam power density and consequently, the penetration.

Xiao et al. [10] studied characteristics of plume and plasma during laser welding of pure iron by a 2.8 kW in fiber laser and CO_2 laser. They concluded that the characteristics of plume and plasma are obviously different. Their measurements confirm that the major attenuating factors for fiber laser welding are principally the scattering and the absorption by the fine fume particles

Fig. 3. High-speed images showing behaviour of molten pool and keyhole as a function of fiber laser power.

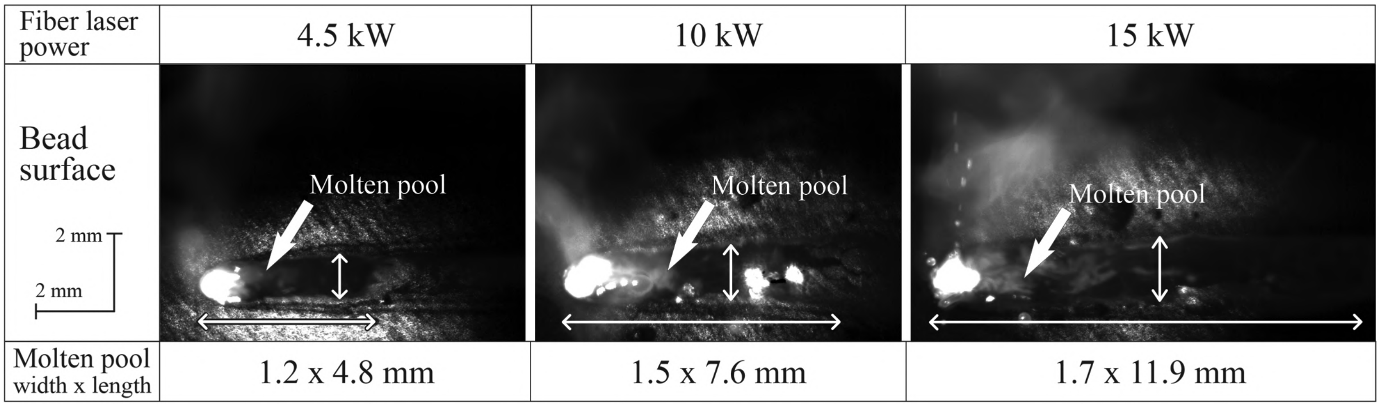

that pass along the path of the laser beam and also the absorption by the plasma plume.

Therefore, the objective of our experiments is to qualify and quantify refraction and attenuation of a 15 kW fiber laser-induced plume, and to measure the electronic temperature and the ionization degree of the laser-induced plasma plume.

2. Experimental setup

The setup used for these experiments is shown in Fig. 1. Experiments were carried out with a 15 kW CW fibre laser (IPG Photonics) of 1.07 μm wavelength and 4.5 mm mrad beam parameter product. The laser beam was delivered through a 200 μm diameter optical fibre. A Precitec YW50 welding head, with a collimating lens and a focusing lens of 150 mm and 300 mm focal lengths, respectively, was used to image the exit of the optical fibre on the specimen surface and, at maximum power, produced a power density of 0.12 MW/mm^2.

Bead-on-plate welds were done on a 25 mm thick 304L stainless steel plate at 3 m/min, with and without a cross jet used at 345 kPa as a side gas. All instruments were stationary while the base material was moved by a robot.

A high-speed video camera was used at 1000 frames per second (fps) to observe the generation of the laser-induced plume, the formation of the keyhole and the formation of the molten pool. The scene was illuminated by a 2 W, 808 nm laser. To indirectly measure the laser beam deviation by the plume, a 1064 nm laser probe was aimed 6.0 mm above the keyhole and directed at a high speed camera at 1.00 m from the keyhole. Also, three laser probes (633 nm He–Ne laser plus 808 and 980 nm diode lasers) were aimed 6.0 mm above the keyhole and directed to a high speed silica detector to indirectly measure the attenuation (diffusion and absorption) levels of laser power due to the plume. The spectrum from the induced plume generated during welding was collected by a high resolution fibre optic Avantes spectrometer (model AvaSpec-3648) with a 0.15 nm spectral resolution and equipped with a 1200 grooves/mm grating and entrance slit size of 10 μm. Plume light was collected by a 50 mm focal length fused silica lens and focused on the optical fibre used to deliver the emitted light to the slit entry of the spectrometer. This collecting lens was located 1.5 m away from the plume, horizontally to the stainless target. The detectable spectral range of the spectrometer was between 230 and 460 nm.

3. Experimental results and discussion

3.1. Plume and bead characteristics

Typical results concerning the visualization of the laser-induced plume, generated during bead-on-plate welding and the melt dynamics observed with the high-speed camera for variable fibre laser powers, are presented below. Figure 2 shows images extracted from a video sequence captured by the high-speed camera, while the laser was emitting at a power of 15 kW. As one can see, the plume behaviour was very unstable in height, width, and direction. The melt at the back side of the keyhole was blown out from the keyhole to form spatters. It was possible to see, on high speed video, the displacement of small spatters toward the keyhole that indicates a Ventury effect at the base of the plume.

Figure 3 shows high-speed video images of the molten pool at different laser power levels. It can be seen that the turbulence and the width and length of the weld pool are increasing with the fibre laser power.

Fig. 4. Distribution of 1064 nm wavelength laser probe beam passing through 15 kW fiber laser-induced plume without side gas.

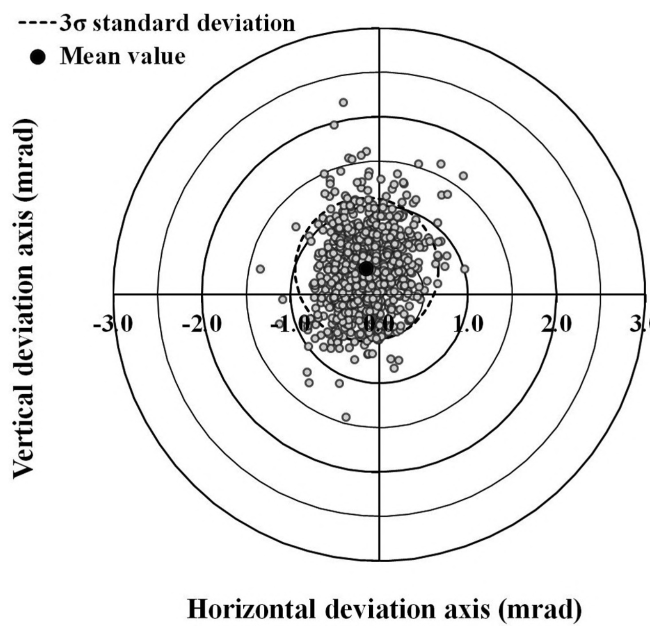

3.2. Laser probe refraction

To indirectly measure the beam refraction, a 1064 nm wavelength laser probe was aimed through the plume and directed to a 2000 fps high speed camera. The intensity centroid of the laser probe was extracted from each frame taken during the weld, to measure the refraction of the laser probe. Figure 4 shows the

Fig. 5. Temporal evolution of a 980 nm wavelength laser probe beam going through laser-induced plume.

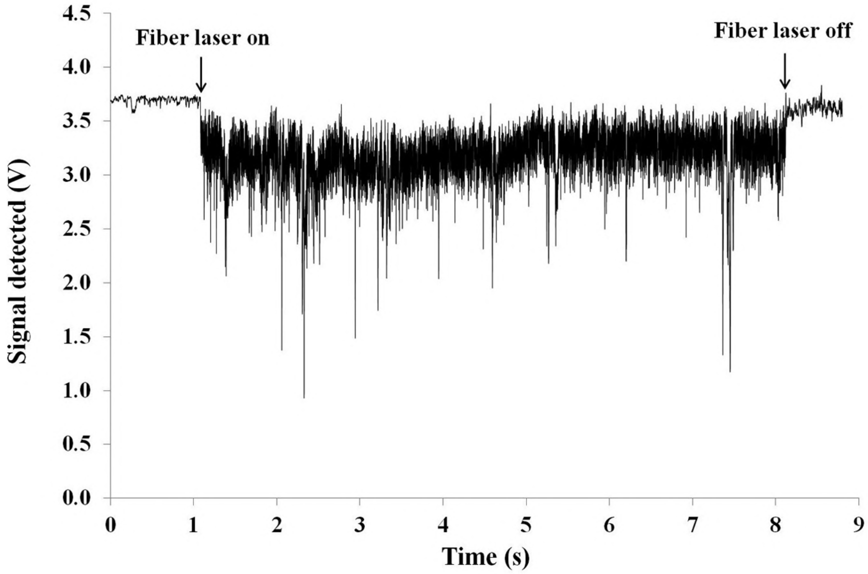

Fig. 6. Attenuation of different wavelength laser probe beams as a function of fiber laser power.

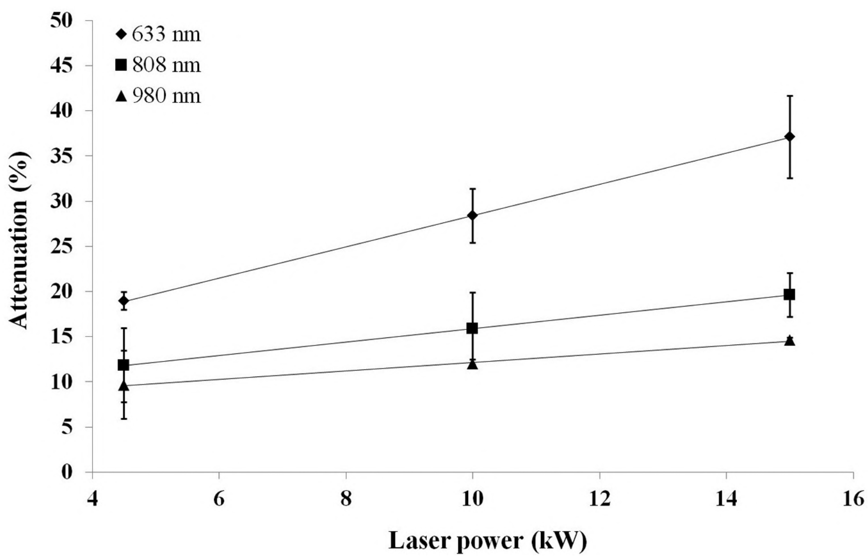

compilation of intensity centroid during a 15 kW weld without side gas. The mean value and the 3σ standard deviation are calculated from the scatter plot. The reference threshold is determined by a laser probe deviation of 10 mrad that represents a displacement of the main laser beam focal point by a distance equal to its radius. The result shows, in the worst case, a refraction of 0.92 mrad where the reference threshold is not reached. The result with side gas drops to 0.35 mrad.

3.3. Laser probe attenuation

Figure 5 shows a typical graph of the transmitted laser probe power at a wavelength of 980 nm and passing through the laser-induced plume as a function of time when the 15 kW fibre laser beam hits the stainless steel plate. Clearly, the transmitted laser probe power drop is quite strong when no side gas is used. These fluctuations are due to the strong instability of the plume. The following equation was applied to calculate the attenuation of the laser probe beam:

$$A = 100\left(\frac{\Phi_{in} - \Phi_{ave}}{\Phi_{in}}\right)$$

where Φ_{in} and Φ_{ave} represent the incident power and the average value of the transmitted power, respectively. In this way, the graph shown in Fig. 6 was obtained. A linear variation of the attenuation, as a function of the fibre laser power, is obvious. Also, plotting the attenuation of the laser probe power as a function of λ^{-4}, leads to the graph shown in Fig. 7. For each of the data points in this graph, three measurements were made and the corresponding average value was plotted. The attenuation appears as a linear function of $1/\lambda$ [4], which indicates a Rayleigh scattering phenomenon.

Fig. 7. Attenuation of different wavelength laser probe beams caused by laser-induced plume.

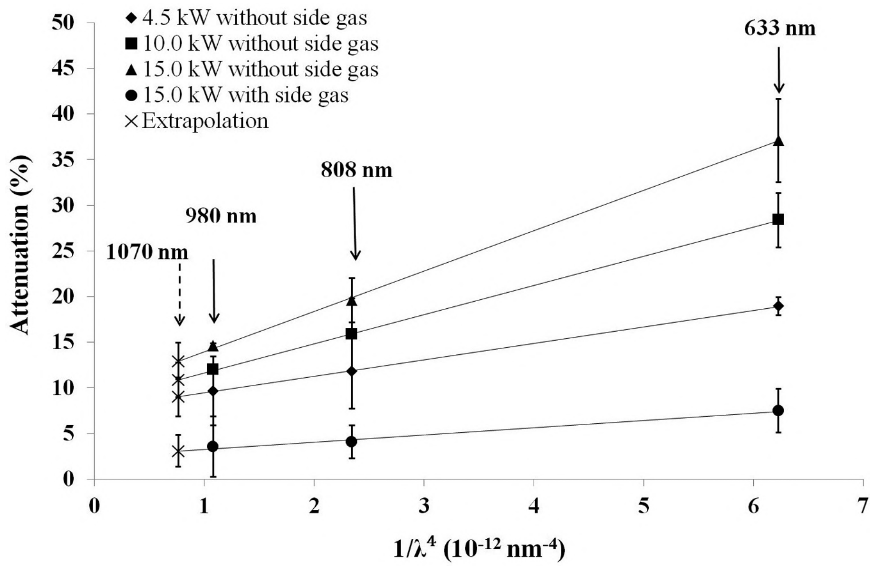

Fig. 8. Emission spectra of stainless steel welding with a 15 kW fiber laser.

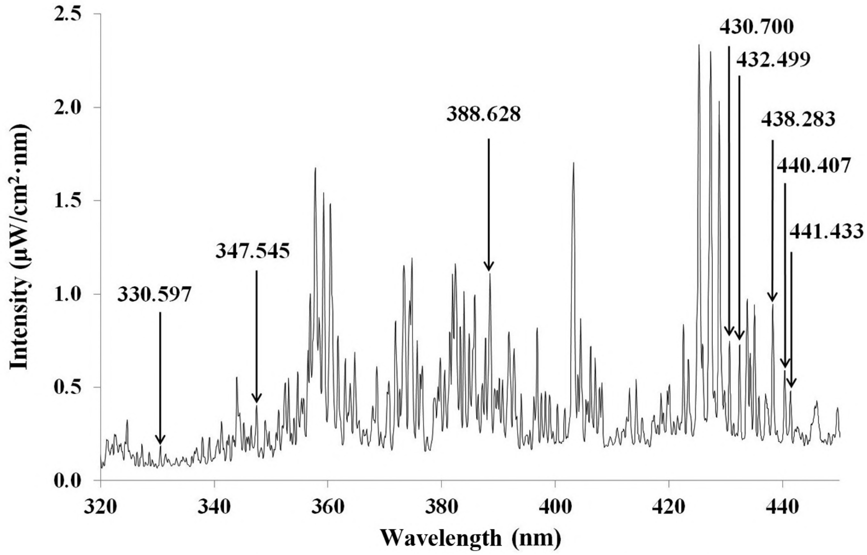

Without side gas, the extrapolated attenuation at the fibre laser wavelength and at 15 kW was 13 ± 2%. With the use of side gas to blow away the induced plume, the attenuation dropped to 3 ± 2%.

3.4. Spectroscopic measurements

From the theory of atomic emission spectroscopy, the plasma temperature is estimated by the relative emission intensities of spectral lines. This electronic temperature is deduced by the Boltzmann plot method, under the local thermodynamic equilibrium assumption. The excited population follows the Boltzmann distribution

$$\ln\left(\frac{I_{mn}\lambda_{mn}}{g_m A_{mn}}\right) = \ln\left(\frac{Nhc}{Z}\right) - \frac{E_m}{kT}$$

where I_{mn}, λ_{mn}, A_{mn}, and g_m represent the relative spectral intensity, wavelength, transition probability of spontaneous emission, and degeneracy of the excited level, respectively; Z is the partition function; N is the atomic number density; h is Planck's constant; c is the speed of light; E_m is the upper state energy level; k is the Boltzmann constant; and T is the electron temperature. As illustrated in Fig. 8; the emission spectrum of the laser-induced plume,

Table 1. Spectroscopic parameters of Fe I lines.

Wavelength, λ (nm)	Transition probability, A (×10^8 s^{-1})	Degeneracy, g	Upper level energy, E (eV)
330.597	0.405	7	5.947
347.545	0.0975	5	3.65
388.628	0.0529	7	3.24
430.790	0.338	9	4.43
732.576	0.516	7	4.47
438.354	0.5	11	4.31
440.475	0.275	9	4.37
441.512	0.119	7	4.42

Fig. 9. Boltzmann plot for the electron temperature based on Fe I emission lines. Lozenges represent experimental data and the line the best fit.

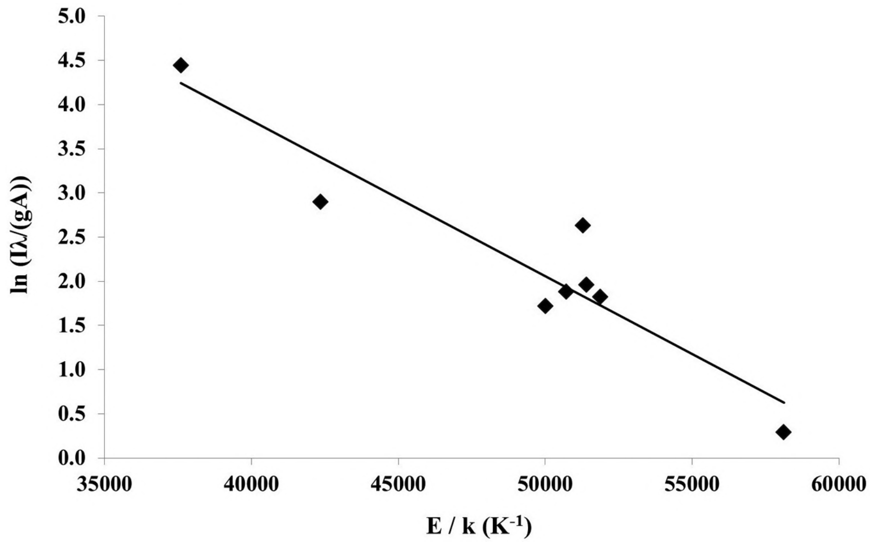

Fig. 10. Temperature dependence of Fe ionization degree, based on Saha's equation.

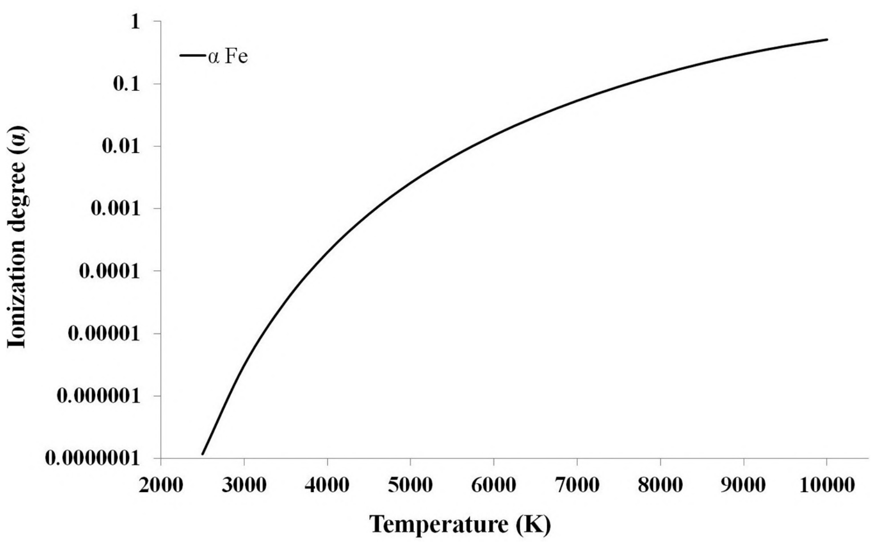

obtained during the welding process at 15 kW, consists of several spectral lines and continuum radiation. Peaks of measured intensities of the Fe I spectral lines together with their spectroscopic parameters, were taken from the NIST atomic database [19] and are summarized in Table 1. The corresponding Boltzmann plot of eight Fe I spectral lines of this spectrum, is shown in Fig. 9. The electronic temperature was calculated at 4.5, 10, and 15 kW, and the results are 5000 ± 300, 5300 ± 100, and 5600 ± 100 K, respectively, without side gas. With side gas, the calculated temperatures are 5100 ± 100, 5400 ± 100, and 8000 ± 2000 K. Subsequently, Saha's equation shown below was applied to calculate the ionization degree of iron

$$\frac{\alpha^2}{1-\alpha^2} = \left(\frac{2\pi m}{h^2}\right)^{3/2} \frac{(kT)^{5/2}}{p} \exp\left(\frac{-qV_i}{kT}\right)$$

where α, m, V_i, q, and p represent the ionization degree, the mass of the electron, the ionized voltage of gas, the electronic charge, and gas pressure, respectively. Assuming that p is 101 kPa and taking the first ionization potential of iron as 7.87 V, one obtains an ionization degree of the plume of 0.8 ± 0.1% at 5600 ± 100 K. For 8000 ± 2000 K one obtains an ionization degree range between 2% and 50% where 10% is calculated from 8000 K. Figure 10 presents the relation of the ionization degree of iron with electronic temperature. The different results are explained by the absorption of the central emission by the peripheral fume. The use of the side gas exposes the center of the plume, which emits intensity wavelengths different from those of the plume peripheral surface. At 4.5, 10, and 15 kW, the peripheral plume is colder and more stable in temperature with a low ionization degree. At 4.5 and 10 kW, the plume center temperature and ionization degree are similar to peripheral plume. However, at 15 kW, the plume center temperature soars with large fluctuations where the ionization degree may vary drastically. At 15 kW, the power density of the beam is 0.12 MW/mm² and the plume should theoretically progress to an ionization state. Consequently, a progression to laser-induced plasma is suspected in the plume center. In the presence of this plasma progression, it is possible to reach IB absorption with the 1070 nm laser.

4. Conclusion

The laser-induced plume has been characterized during bead-on-plate welding of an austenitic stainless steel plate with a 15 kW fibre laser beam. The images captured with a high-speed video camera showed that the plume behaviour was very unstable when the laser-induced plume was not blown by a side gas jet. The use of a side gas blows away the fume at the top of the keyhole and stabilises the induced plume. Also, from the differences observed between the series of frames, some changes can be seen in the shape of the melt pool. The results confirm that the width of the melt pool increases as a function of the fiber laser power.

Measurements of the deviation confirm that the beam is not significantly deviated and that penetration should not be affected by this factor.

Attenuation measurements of the laser probe power by the induced plume indicated that the laser power is not entirely reaching the target surface. The fibre laser output power intensity, across the irradiated spot, is modified by the plume. At 15 kW, this appears as a 13% reduction, in incident laser power density, at a plane 6.0 mm above the specimen surface. Using the side gas decreases the attenuation to 3%. Moreover, the main attenuation factor is attributed to Rayleigh scattering in the relationship between attenuation and wavelength represented by a dependence of λ^{-4}.

Spectroscopic measurements showed that a focused 15 kW fiber laser beam produced a partially ionized plume. The temperature and ionization degree of the 15 kW laser- induced plume without side gas were calculated to be 5600 K and 0.8%, respectively, by using Boltzmann plot method and Saha's equation. Using the side gas, the temperature and the ionization degree are 8000 K and 10%, respectively. This temperature variation is explained by the difference in temperature of the peripheral plume and the plume center exposed by the side gas. The high temperature and the large fluctuation of the plume center lead to a drastic variation of the ionization degree and progression to laser-induced plasma is suspected. IB absorption is possible in presence of this progression.

References

1. M.V. Allmen. Laser-Beam Interactions with Materials. Springer-Verlag, Berlin, Heidelberg, New-York, London, Paris, Tokyo. 1987.
2. A.M. Prokhorov, V.I. Konov, I. Ursu, and I.N. Mihailescu. Laser heating of metals. Adam Hilger, Bristol, Philadelphie and New-York. 1990.
3. J. Dowden. The theory of laser materials processing. Springer Science. 2009. pp. 71–128.
4. F.O. Olsen. Hybrid laser-arc welding. Woodhead Publishing Limited, Oxford, Cambridge, New Delhi, and CRC Press, Boca Raton, Boston, New York, Washington, DC. 2009.
5. E. Kannatey-Asidu, Jr. Principles of Laser Materials Processing. John Wiley & Sons, Inc. Hoboken, New Jersey. 2009. pp. 515–521.
6. P. Schaaf. Laser Processing of Materials. Springer Science. 2010. pp. 21–88.
7. W.M. Steen and J. Mazumder. Laser Material Processing. Springer Verlag, London. 2010.
8. D. Bäuerle. Laser Processing and Chemistry. Springer-Verlag, Berlin, Heidelberg. 2011.
9. A.F.H. Kaplan and J. Powell. J. Laser Appl. **23**, 032005 (2011). doi:10.2351/1.3597830.
10. R. Xiao and J. Zou. *In* International Congress on Applications of Lasers and Electro-Optics. Anaheim. 2012. [Present by Laser Institute of America, Conference program, p. 82 (1002)].
11. E. Dumord, J.M. Jouvard, D. Grevey, M. Druetta, and P. Ottavi. Journal de Physique III, 1997. pp. 1079–1096.
12. D. Lacroix, G. Jeandel, and C. Boudot. J. Appl. Phys. **84**, 2443 (1998). doi:10.1063/1.368405.
13. J. Greses, P.A. Hilton, C.Y. Barlow, and W.M. Steen. J. Laser Appl. **16**, 9 (2004). doi:10.2351/1.1642636.
14. S. Katayama, Y. Kawahito, K. Kinoshita, N. Matsumoto, and M. Mizutani. Proceedings of the ICALEO 2007. pp. 353–359.
15. Y. Kawahito, K Kinoshita, N. Matsumoto, M. Mizutani, and S. Katayama. Sci. Technol. Weld. Joining, **13**(8), 749 (2008). doi:10.1179/136217108X356971.
16. Y. Kawahito, N. Matsumoto, M. Mizutani, and S. Katayama. Sci. Technol. Weld. Joining, **13**(8), 744 (2008). doi:10.1179/136217108X329313.
17. Y. Kawahito, K. Kinoshita, N. Matsumoto, and S. Katayama. J. Laser Appl. **21**(2), 96 (2009). doi:10.2351/1.3110058.
18. S. Oiwa, Y. Kawahito, M. Mizutani, and S. Katayama. J. Laser Appl. **23**(2), 022007 (2011). doi:10.2351/1.3567959.
19. The National Institute of Standards and Technology (NIST). NIST Atomic Spectral Database. http://physics.nist.gov/PhysRefData/contents.html.